Effect of Heat Treatment Conditions on Corrosion and Hydrogen Diffusion Behaviors of Ultra-Strong Steel Used for Automotive Applications

Jin-seong Park[1], Hwan Goo Seong[2], and Sung Jin Kim[1,†]

[1]*Department of Advanced Materials Engineering, Sunchon National University, Sunchoen 57922, Korea*
[2]*POSCO Technical Research Laboratories, Pohang 37673, Korea*

The purpose of this study was to examine the influence of conditions for quenching and/or tempering on the corrosion and hydrogen diffusion behavior of ultra-strong automotive steel in terms of the localized plastic strain related to the dislocation density, and the precipitation of iron carbide. In this study, a range of analytical and experimental methods were deployed, such as field emission-scanning electron microscopy, electron back scatter diffraction, electrochemical permeation technique, slow-strain rate test (SSRT), and electrochemical polarization test. The results showed that the hydrogen diffusion parameters involving the diffusion kinetics and hydrogen solubility, obtained from the permeation experiment, could not be directly indicative of the resistance to hydrogen embrittlement (HE) occurring under the condition with low hydrogen concentration. The SSRT results showed that the partitioning process, leading to decrease in localized plastic strain and dislocation density in the sample, results in a high resistance to HE-induced by aqueous corrosion. Conversely, coarse iron carbide, precipitated during heat treatment, weakened the long-term corrosion resistance. This can also be a controlling factor for the development of ultra-strong steel with superior corrosion and HE resistance.

Keywords: Ultra-strong steel, Heat treatment, Corrosion induced hydrogen diffusion, Residual stress, Carbides

1. Introduction

Owing to the stricter international restrictions on CO_2 emissions and auto-safety, the weight reduction of auto-parts is becoming a major technical issue in the automotive industry [1-4]. Among the various technical strategies, the use of ultra-strong steel with a tensile strength exceeding 2 GPa is proposed because it ensures an effective weight reduction of cars without a decrease in the passenger safety [5-7]. In the application of ultra-strong steel to auto-parts, however, there is a critical challenge that can be overcome, i.e. stronger steel is more vulnerable to corrosion [8] and hydrogen embrittlement (HE) than softer steels [9,10]. In general, stronger ferritic steels with higher C contents have a larger fraction of iron carbide [2]. From an electrochemistry point of view, the carbide acts as a cathode, and an increase in its fraction can promote anodic dissolution of the matrix ($Fe \rightarrow Fe^{2+} + 2e^-$) [11]. Moreover, when steel is exposed to an aqueous environment, H evolution and entry processes, which are

strongly dependent on the pH, are involved. The followings are the proposed H evolution reactions [12,13].

Hydrogen reduction: $H^+ + e^- \rightarrow H$ (1)

Hydrolysis: $Fe^{2+} + H_2O \rightarrow Fe(OH)_2 + 2H^+$ (2)
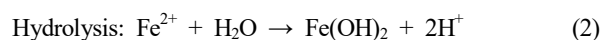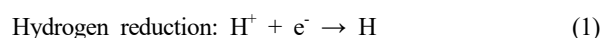
H atoms absorbed on the steel surface can diffuse through the steel matrix and they can be trapped at some metallurgical defects with high energy, which impairs the ductility and accelerates the embrittlement phenomena [14-16]. Although there are a considerable number of reports concerning the influence of alloying elements on the HE of steel [17-19], most of them focused on the mechanical degradation of pre-charged steel under electrochemical cathodic polarization, and the corrosion behaviors on the steel surface were not considered. In particular, there have been a limited number of studies on the effects of microstructural modifications by heat treatment on the corrosion and HE of ultra-strong automotive steel. Therefore, this study examined the corrosion-induced HE of ultra-strong steel samples prepared under different heat treatment conditions, and the controlling factors for corro-

---

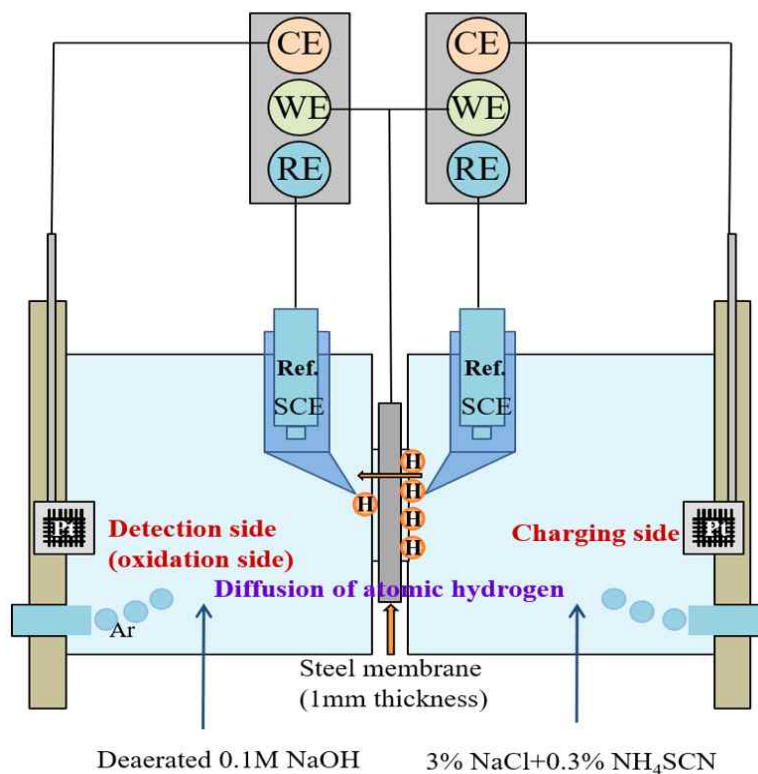†Corresponding author: sjkim56@scnu.ac.kr

Fig. 1 Schematic diagram of the electrochemical hydrogen permeation apparatus.

sion-induced HE are provided.

2. Experimental

2.1 Specimen preparation and microstructure observation

The test steel used in this study was ultra-strong ferritic steel consisting primarily of 0.4 ~ 0.5 wt% C, 1 ~ 1.5 wt% Mn, and 0.2 ~ 0.3 wt% Si. The samples were re-heated to 1200 ℃ for 2 h, and hot rolled and then cold rolled to a 2 mm thickness. The samples were then auste-nitized by heating to 930 ℃ for 7 min and quenched in two types of quenchant: water, and a mixture of oil and water. The two types of sample, which had been quenched in water (WQ) and a mixture of oil and water (OQ) were additionally tempered at 200 ℃ for 30 min (WQT) and 45 min (OQT$_1$), respectively. A different tempering con-dition of 70 ℃ for 1 h was also applied to the OQ sample (hereinafter referred to as OQT$_2$). In addition, the austenitized sample was immersed in a molten salt bath at 350 ℃ for 15 s, and transferred immediately to another salt bath at 400 ℃ for 10 min, and finally cooled in air. This heat treatment condition was selected based on the two-step partitioning process [20]. This sample is simply referred to as AT.

For microstructural observations, the test specimens were polished with a final polishing step of 1 μm and etched with a 5% nital solutions. The microstructures were then examined by field emission-scanning electron micro-scopy (FE-SEM). The morphological features of the pre-cipitates in the microstructure were examined by TEM using thin foil and extraction replica specimens.

2.2 EBSD-KAM analysis

The extent of the misorientation of the quenched and tempered specimens was measured by electron backscatter diffraction (EBSD)-kernel average misorientation (KAM) using TSL software (version 7.0). For EBSD analysis, the acceleration voltage, beam current, working distance, tilt angle, and step size were 20 kV, 1 nA, 15 mm, 70º, and 100 nm, respectively.

2.3 Electrochemical hydrogen permeation test

To understand the physical nature of H diffusion in the steel specimens, electrochemical permeation tests in reference to the ISO 17081 [21] standard were conducted. Fig. 1 pres-ents a schematic diagram of the electrochemical H per-meation test apparatus. In the H permeation test (HPT), H atoms, which were reduced on the steel surface in the H charging side, diffused through the steel membrane and
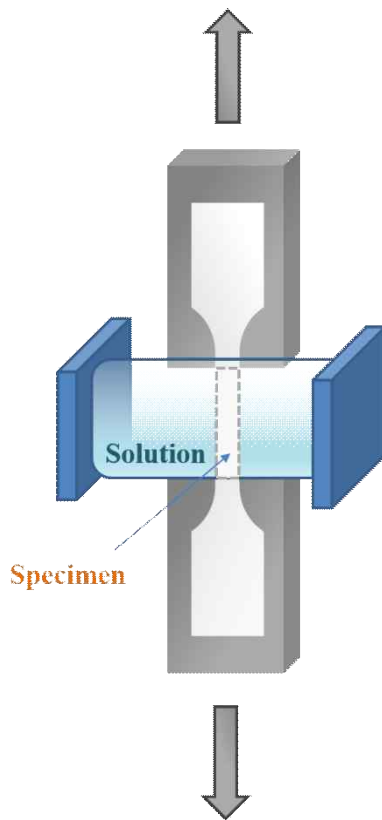
Fig. 2 Schematic diagram of the SSRT apparatus.

the H permeation flux was obtained by measuring the H oxidation current density in the H detection side. For this, Pt foil and saturated calomel electrode (SCE) were used as the counter and reference electrodes, respectively. The sheet-type steel membrane with a 1 mm thickness that was polished mechanically to #2000 grade was placed in center of the permeation cell. To improve the oxidation efficiency of the H atoms, Pd plating was performed on the steel surface in the detection side by galvanostatic polarization at a constant charging current of - 2.8 mA/cm^2 for 180 s in 500 mL of an ammonia + 2.54 g PdCl$_2$ solution. The circular area of the specimen exposed to the electrolyte was 3.14 cm^2. The specimen in the charging side was polarized galvanostatically at a constant charging current density of -1 mA/cm^2 in a 3.5% NaCl + 0.3% NH$_4$SCN solution. The galvanostatic current density was selected in reference to the previous studies [2,22]. The specimen in the detection side was potentiostatically polarized at a constant potential of 270 mV versus the SCE in a deaerated 0.1M NaOH solution. The anodic current density over time until reaching a steady-state value, i_{ss} (μA/m^2), was measured to determine a range of diffusion parameters, D_{app} (m^2/s, diffusivity), $J_{ss}L$ (mol/m·s, perme-

ability), and C_{app} (mol/m^3, solubility) using the break-through time method derived from Fick's second law, which are expressed as follow:

$$D_{app} = L^2 \, / \, (15.3 \cdot t_{bt}) \tag{3}$$

$$J_{ss}L = i_{ss}L \, / \, nF \tag{4}$$

$$C_{app} = J_{ss}L \, / \, D_{app} \tag{5}$$

where t_{bt} is the time needed for H atoms to begin arriving at the detection side; L is the thickness of the steel membrane; i_{ss} is the steady state H permeation current; n is the number of electrons transferred and F is the Faraday constant (C/mol).

2.4 Slow strain rate tensile (SSRT) test and fractography analysis

To evaluate the resistance to corrosion-induced HE, SSRT [23] at a strain rate of 1×10^{-6}/s was conducted in air and Walpole solution (0.2 M CH$_3$COONa + 0.185 M HCl) at room temperature. The specimens were 80 mm in gauge length, 6 mm in width, 1mm in thickness and 12 mm in diameter. Fig. 2 shows a schematic diagram of the test apparatus. The sensitivity of HE (HE index), indicating the degree of mechanical degradation by exposure to the corrosive environment, was quantified as follows:

$$\text{HE index (\%)} = (1 - \frac{W_s}{W_a}) \times 100 \tag{6}$$

where W_a and W_s are the mechanical testing parameters (tensile strength, elongation) measured in air and Walpole solution, respectively.

The fracture morphologies after SSRT were observed by FE-SEM. The fracture surfaces were divided into three different fracture modes, micro-dimple (MD), quasi-cleavage (QC), and intergranular (IG) patterns; and the fraction of each fracture mode was presented quantitatively.

2.5 Electrochemical polarization test and long-term immersion test

To evaluate the corrosion resistance of the samples, a potentiodynamic polarization test at a scan rate of 0.2 mV/s was performed in a Walpole solution. Pt foil and saturated calomel electrode was used as the counter and reference electrodes, respectively.

An immersion test in a 3.5% NaCl solution for four weeks was conducted to examine the long-term corrosion behaviors on the surfaces, and the corrosion weight loss of the samples was measured. Cross-sections of the scale
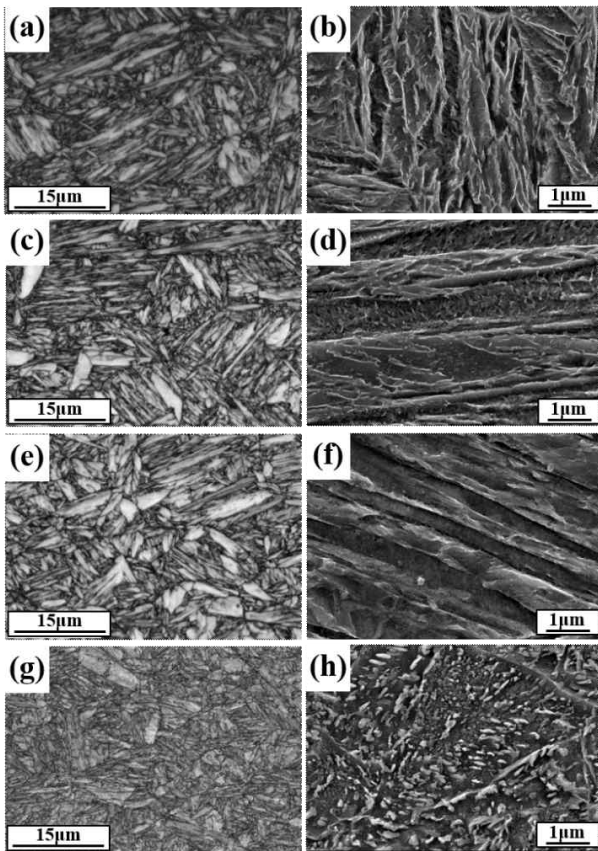
Fig. 3 Microstructure observed by EBSD (a, c, e, g) and FE-SEM (b, d, f, h): (a-b) WQT, (c-d) OQT₁, (e-f) OQT₂, and (g-h) AT samples.

formed on the sample surfaces after the immersion test were prepared using a focused ion beam (FIB) and observed by TEM. To measure the corrosion weight loss of the samples, the specimens, 50 mm in width, 60 mm in length, and 1 mm in thickness, were cleaned with ethanol and weighed on an electronic balance to a precision of 0.0001 g. After the immersion test, the samples were cleaned ultrasonically in ethanol for 2 min to remove the scale completely. The samples were weighed again on the same balance. The difference between the initial and final weights divided by the initial surface areas was defined as the corrosion weight loss of the sample.

3. Results and discussion

3.1 Microstructure observation and KAM analysis

Fig. 3 presents the microstructures of the steel samples after heat treatment (quenching and tempering), which were observed by EBSD and FE-SEM. The WQT, OQT_1, and OQT_2 samples were composed of lath-type martensite, whereas the AT sample had the bainitic structure. Because tempering for the WQT and OQT_1 samples was conducted at 200 °C, it can be expected that iron carbide in a form of ε-$Fe_{2.4}C$ was precipitated in the microstructure [24]. The need-shaped fine carbides, less than 200 nm in size, which had been precipitated in the martensite lath during tempering, was clearly observed by TEM (Fig. 4a). According to previous studies [24-26], it is considered that the main precipitates contained in the martensitic steel that had been tempered at or below 200 °C were ε-$Fe_{2.4}C$, not Fe_3C. Although the precipitates were so fine that a clear diffraction pattern was not obtained, it is reasonable to consider that the fine precipitates contained in the two samples were ε-$Fe_{2.4}C$. Morphological observations of the OQT_2 sample (Fig. 3e-f) showed that the precipitation of fine carbide was almost excluded after tempering below 100 °C. On the other hand, the circular-shaped coarse carbides were precipitated in the bainitic structure of the AT
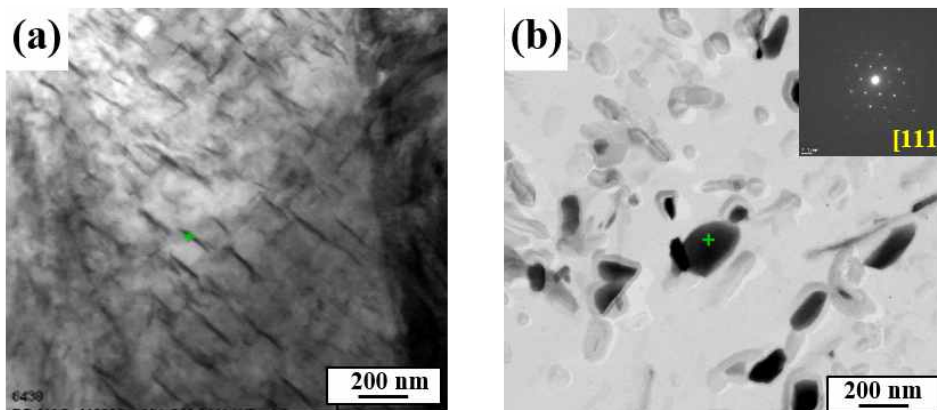

Fig. 4 TEM observation: (a) fine needle shaped ε-$Fe_{2.4}C$ in the WQT sample and (b) coarse spherical shaped Fe_3C in the AT sample.

Table 1 Hydrogen diffusion parameters of the four tested samples

	Time (s)	D_{app} (m^2/s)	$J_{ss}L$ (mol/m·s)	C_{app} (mol/m^3)
WQT	t_{bt}: 1839.951	9.094×10^{-11}	8.441×10^{-10}	9.282
OQT$_1$	t_{bt}: 2105.949	8.170×10^{-11}	6.718×10^{-10}	8.223
OQT$_2$	t_{bt}: 2233.946	7.631×10^{-11}	6.719×10^{-10}	8.805
AT	t_{bt}: 1525.962	1.107×10^{-10}	1.146×10^{-9}	10.352
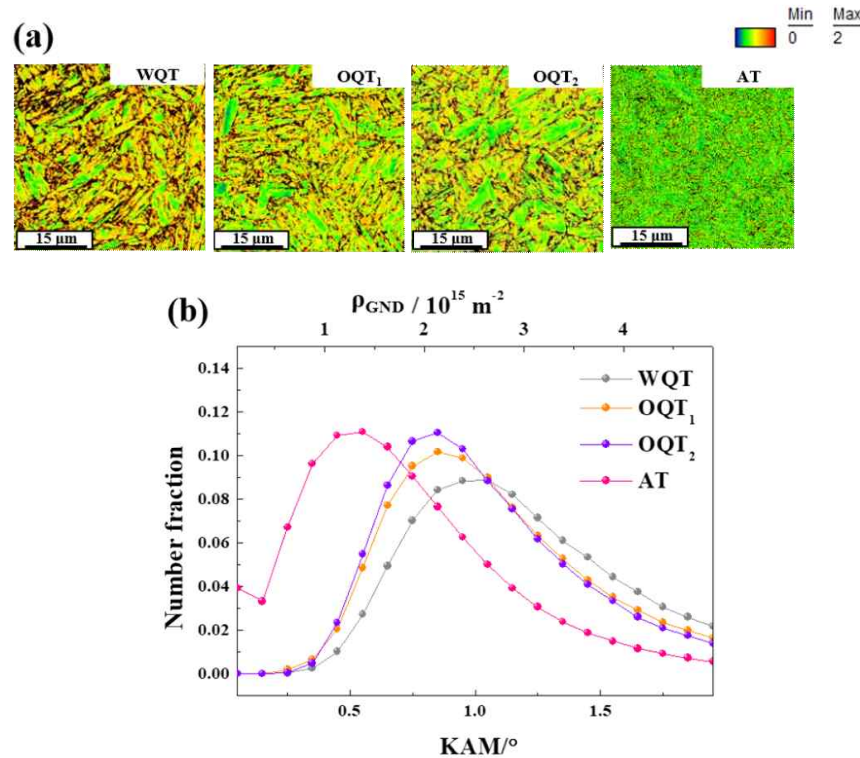
Fig. 5 (a) KAM maps and (b) KAM frequency distribution curves of the four tested samples.

sample, as shown in Fig. 4b. They were characterized as Fe$_3$C, which is considered a stable carbide that precipitates during partitioning above 260 $^{\circ}$C [27], from the electron diffraction pattern from TEM. Fig. 5a-b shows the KAM analysis results obtained by EBSD measurements of the samples. The level of localized plastic strain can be measured indirectly because KAM is the average misorientation angle of the point with the all neighboring points. In addition, geometrically necessary dislocations (GNDs) are stored dislocations that were formed to accommodate the lattice curvature during non-uniform deformation [28], and they are closely associated with the KAM data. The density of GND (ρ_{GND}) can be quantified indirectly from the KAM data using the following equation [28].

$$\rho_{GND} = \frac{1.5\gamma\vartheta}{ub} \qquad (7)$$

where ϑ, u, b, and γ are the misorientation angle associated with ρ_{GND}, step size, Burgers vector, and constant depending on the geometry of the boundaries, respectively. As shown in Fig. 5a-b, the misorientation angle and dislocation density increased in the order of AT, OQT$_1$ ≈ OQT$_2$, and WQT, with WQT being the highest. From this result, it is expected that the critical factor for the level of localized plastic strain during the thermal treatment was the cooling rate in the quenching process. Considering that H atoms in steel can diffuse preferentially to a high stress field [29,30] (i.e. stress-induced H diffusion), the H diffusion behaviors and embrittlement properties in the tested samples can differ according to the levels of localized
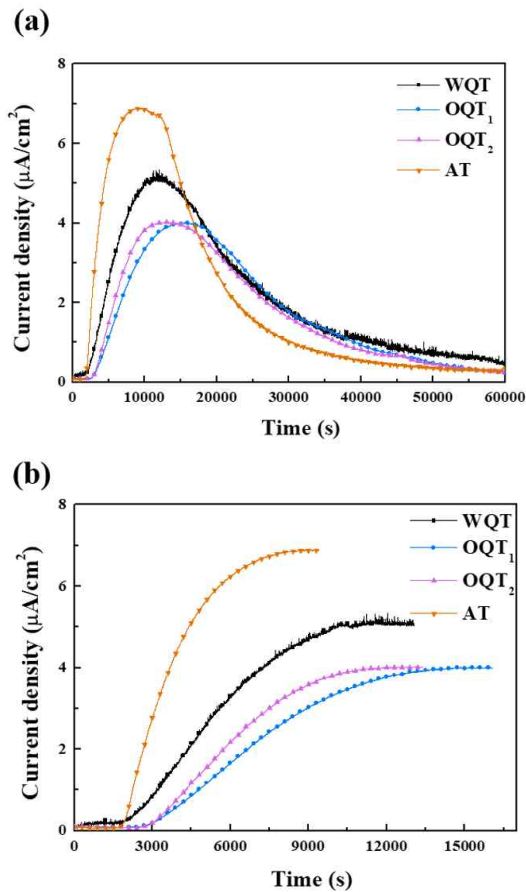
(a)

(b)

Fig. 6 (a) H permeation curves of the four tested samples, and (b) their rising permeation transients.

plastic strain and dislocation density. This is discussed in more detail in the following section.

3.2 Electrochemical hydrogen permeation test

Fig. 6a-b presents the H permeation behaviors in the tested samples; Table I lists several diffusion parameters obtained from equations (3), (4), and (5). Compared to the AT sample composed of bainite, the WQT, OQT_1, and OQT_2 samples composed of martensite or tempered martensite with relatively higher residual stress showed much lower H diffusivity and permeability. T difference in the H diffusion characteristics among the samples tested could be attributed mainly to the difference in the parameters considering the previous investigations reporting that the H diffusion and trapping behaviors can be strongly dependent on the three types of metallurgical parameters, the level of residual stress, dislocation density, and carbide precipitated in the microstructure [2,30]. Based on previous studies [31-33], the H-binding energy with dislocation and Fe_3C was 23-27 kJ/mol and 11-18 kJ/mol,

respectively. This suggests that they can be regarded as reversible H traps, resulting in slower diffusion kinetics for H atoms. The much higher H diffusivity of the AT sample can be understood by the much lower dislocation density which was estimated indirectly by the localized plastic strain from KAM analysis (Fig. 5). On the other hand, the coarse Fe_3C particles distributed in the AT sample had a comparatively lesser effect on the delay of H diffusion. As reported previously [34], the growth and agglomeration of Fe_3C in the steel during heat treatment can provide a lower interfacial area for H trapping, suggesting that the H trapping efficiency can be decreased. In contrast, the WQT, OQT_1, and OQT_2 samples, which were composed of martensite or tempered martensite with relatively higher dislocation densities and fine ε-$Fe_{2.4}C$ particles, showed much lower diffusion kinetics of H atoms. In particular, in contrast to Fe_3C, fine ε-$Fe_{2.4}C$ with a H-binding energy of 65 kJ/mol [31,35] can contribute to the much slower diffusion kinetics of H atoms. As reported previously [36], the coherency or semi-coherency of ε-$Fe_{2.4}C$ with the matrix can have a strain field that can draw and pin H atoms, delaying H transport. Compared to the WQT sample with higher residual stress, the OQT_1 sample with a higher fraction of ε-$Fe_{2.4}C$ showed a lower D_{app}, which can be understood in this
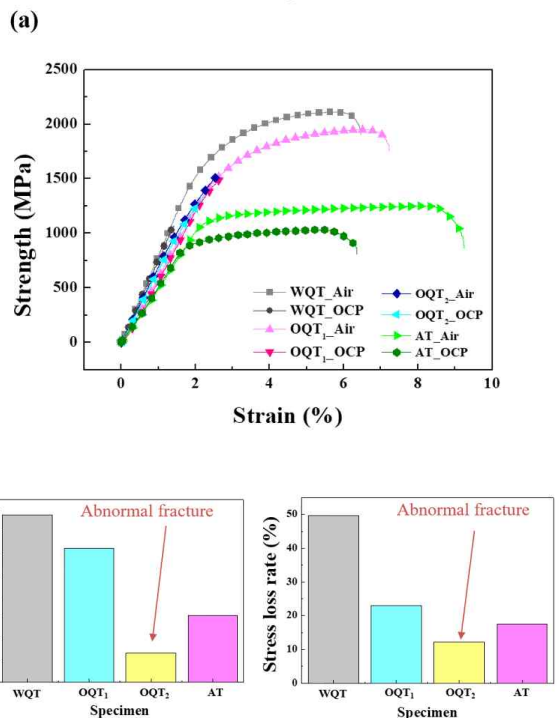
(a)

(b)

Fig. 7 SSRT results: (a) engineering stress-strain curves of the four tested samples, evaluated in air and Walpole solution, and (b) reduction rate of mechanical testing parameters (stress and strain).
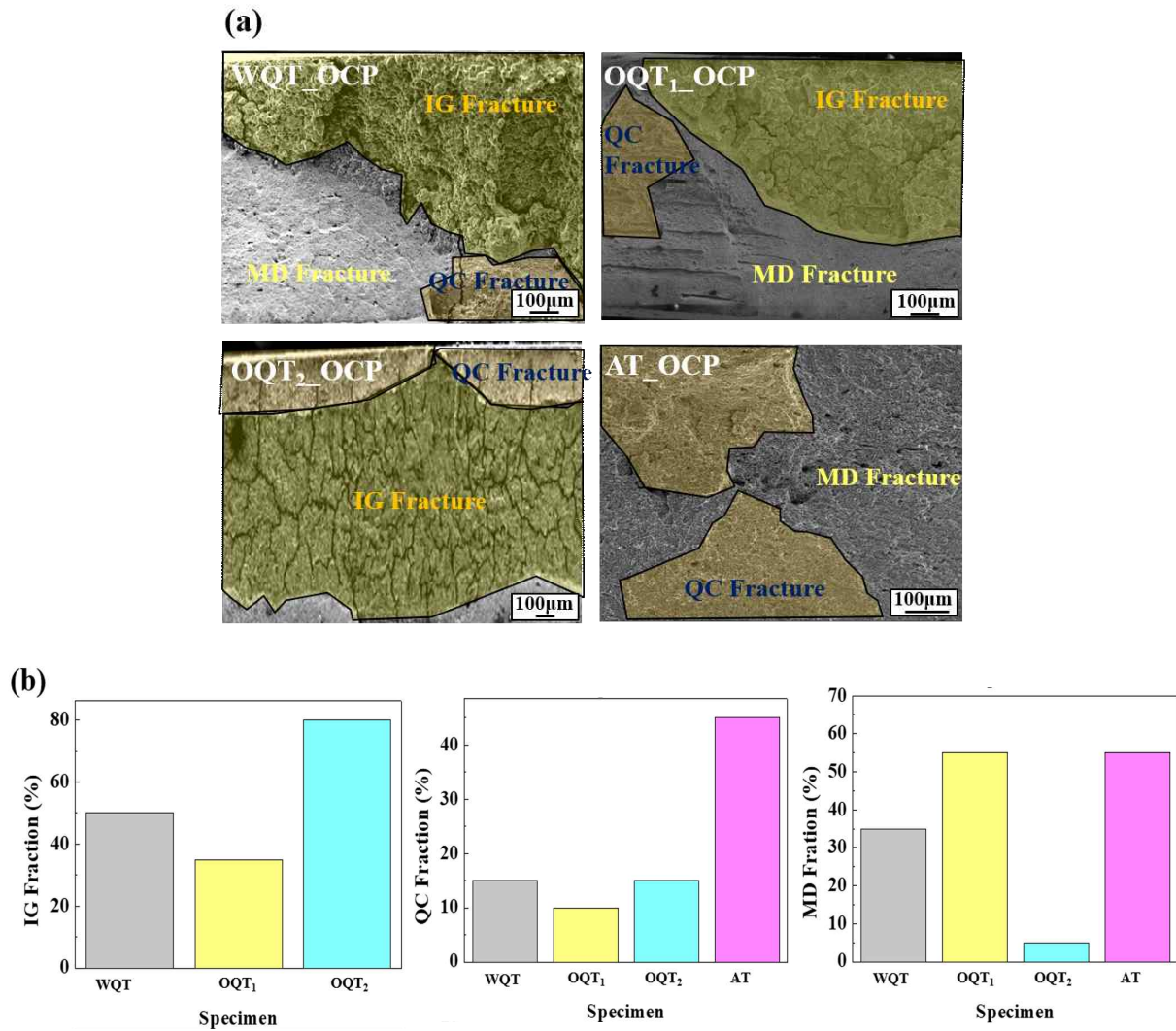
Fig. 8 (a) Fracture surfaces of the four tested samples after SSRT, evaluated in a Walpole solution, and (b) fraction of IG, QC, and MD patterns in the fracture surfaces.

regard. Despite the inverse relationship between D_{app} and C_{app}, as found in equation (5), the sub-surface H concentration (regarded simply as H solubility, C_{app}) was increased in the order of $OQT_1 \approx OQT_2$, WQT, and AT with AT being the highest, which may be due to the differ-

ence in the H overvoltage and total fraction of carbide precipitated. Because the H permeation data was obtained under cathodic polarization condition, it was not enough to clearly evaluate the resistance to HE-induced by aqueous corrosion. Therefore, SSRT was also conducted under a corrosive environment, which is discussed in the following section.

3.3 Slow strain rate tensile test and fractography analysis

Fig. 7 presents the engineering stress-strain curves of the four different sample tested. As shown in Fig. 7a, all samples exhibited a significant decrease in elongation and tensile strength when exposed to a Walpole solution (OCP). In the case of the OQT_2 sample obtained by tempering below 100 ℃, an abnormal fracture occurred even in air.

Table 2 HE indices of the four tested samples

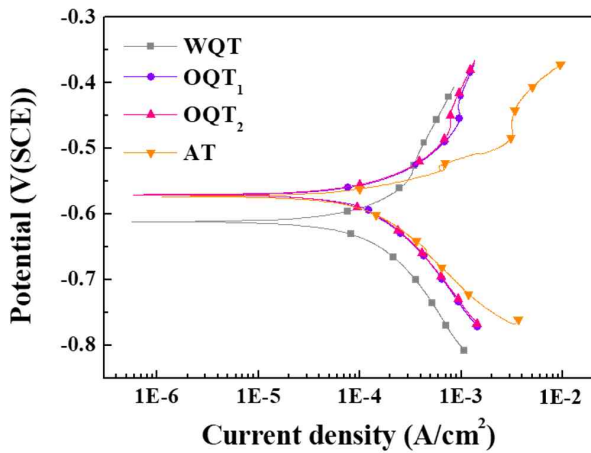|	HE Index (%)	
	Strain	Strength
WQT	77.91	49.62
OQT_1	62.26	22.87
OQT_2	13.51	12.26
AT	31.10	17.44

Fig. 9 Electrochemical polarization test results of the four tested samples.

Table 2 lists the HE-indices of the tested samples that were obtained by the reduction of the mechanical testing parameters. The HE index of the OQT$_1$ sample was lower than that of the WQT sample because of the lower internal residual stress and higher fraction of ε-Fe$_{2.4}$C. In partic-

ular, Kim [37] reported that ε-Fe$_{2.4}$C that precipitated in the martensite lath acted as a deep trap for H and could immobilize partially the diffusible H. The beneficial effects of ε-Fe$_{2.4}$C on the resistance to HE can only be highlighted when the steel is exposed to neutral environments with low H concentration. Fig. 8 shows the fracture surfaces of the samples after SSRT, indicating that the WQT sample showed a slightly higher fraction of IG fracture, which is normally considered H-induced brittle failure, than the OQT$_1$ sample. In the case of the OQT$_2$ sample showing abnormal fracture, the fraction of IG fracture was the highest among the samples. These results suggest that faster quenching rate or lower tempering temperature can lead to higher fraction of IG fracture. Except for the OQT$_2$ sample, the AT sample with the bainitic structure exhibited the lowest HE index and the highest fraction of MD fracture, which appears to be a contradiction with the highest value of C_{app} obtained by the permeation experiment. This suggests that the experimental data obtained from the sample fully charged with H by applying a high cathodic current cannot simulate the embrittlement phenomenon occurring in an actual corrosive environment.
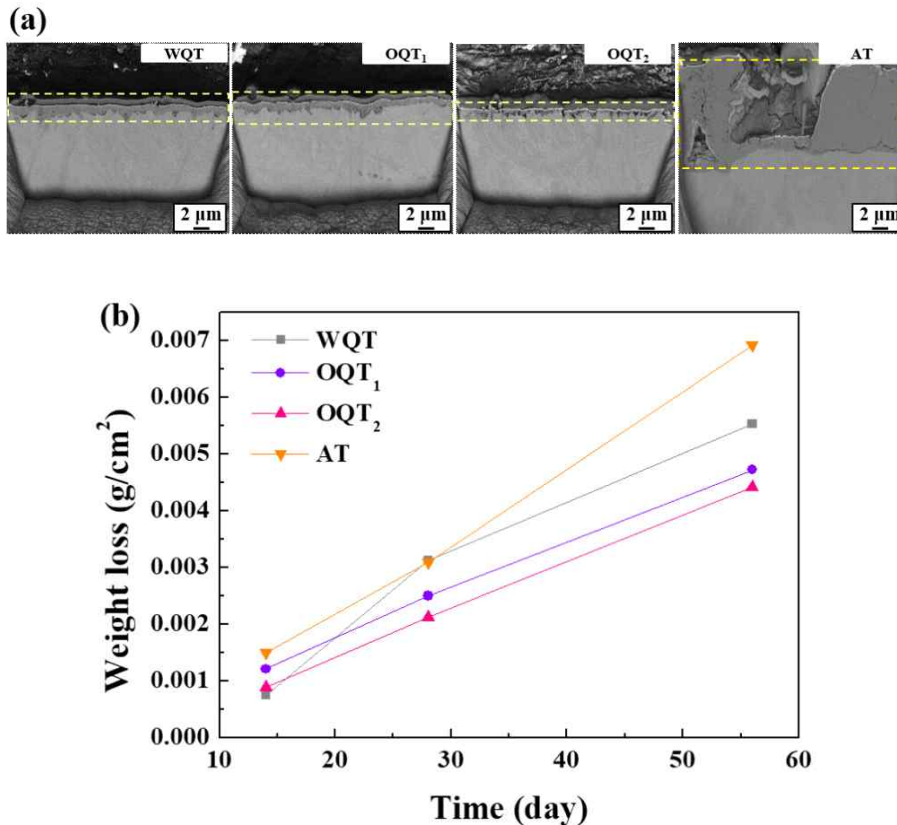

Fig. 10 (a) Cross-sectional views of the corrosion products formed on the four tested samples after the immersion test for four weeks, and (b) their weight loss per unit area.
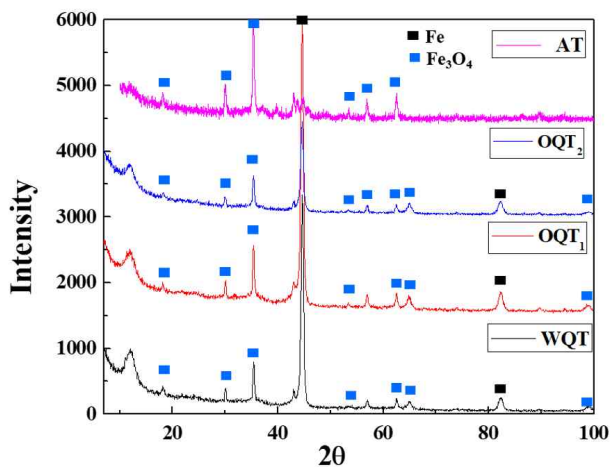
Fig. 11 XRD patterns of the four tested samples after the immersion test for four weeks.

Despite having the lowest HE index, the AT sample could not be regarded as the most promising GIGA steel for automotive applications among the four tested samples for two reasons. One is the significant reduction in the tensile strength below 1.5 GPa, and the other is the inferior corrosion resistance. As shown in Fig 9, the AT sample exhibited the highest current density under anodic polarization. The lowest resistance to aqueous corrosion of the AT sample may be attributed to the high fraction of Fe_3C. Because the carbide is a metallic conductor and acts as a cathode [11], it can promote the selective dissolution of the matrix. Considering that the perforation corrosion is one of the critical technical problems for the steel sheets used for auto parts, the characteristics of the corrosion behaviors should be investigated more clearly. In particular, because there has been a lack of consideration of the aqueous corrosion and corrosion scale, the authors focused on the long-term corrosion characteristics of the tested samples, which will be discussed in the following section.

3.4 Long term corrosion behavior

Fig. 10a shows cross-sectional images of the corrosion scale formed on the surface after immersion in a 3.5% NaCl solution for four weeks. The corrosion scale formed on the AT sample was much thicker (approximately 9 μm) than the other samples, and a significant portion of thick scale was detached. According to the equation proposed by Mullin [38], the rapid precipitation of scale on the surface could have resulted from a larger amount of dissolved Fe cation generated by the higher anodic dissolution rate. This suggests that the AT sample with coarse Fe_3C particles distributed throughout the microstructure

showed the lowest long-term corrosion resistance, and the measured weight losses, as shown in Fig. 10b, were consistent with the polarization measurements (Fig. 9) and cross-section observations (Fig. 10a). On the other hand, the OQT_2 sample with few carbide particles showed the thinnest scale (approximately 1 μm) on the sample surface, and the lowest weight loss. XRD showed that the corrosion scale formed on the surface consisted mainly of Fe_3O_4, which is a non-protective layer for aqueous corrosion [39]. The peak intensity of Fe_3O_4 increased with increasing fraction of iron carbides precipitated in the microstructure, and the highest peak intensity of Fe_3O_4 was observed in the AT sample. Based on these results, it can be assumed that heat treatment for the reduction of H-induced mechanical degradation may not necessarily ensure a high resistance to aqueous corrosion.

4. Conclusion

The controlling factors for the corrosion and corrosion-induced HE of ultra-strong automotive steel were investigated using a range of analytical and experimental methods. The major conclusions were as follows:

1. The quenched and tempered samples (WQT, OQT_1, and OQT_2) were composed of lath-type martensite, whereas the sample (AT) which had been partitioned in the two salt baths had a bainitic structure. Two types of precipitates were formed in the microstructure during the heat treatments: needle-shaped fine $\varepsilon\text{-}Fe_{2.4}C$ and round-shaped coarse Fe_3C. The misorientation angle and dislocation density of the samples, which were measured by EBSD-KAM, increased with the cooling (quenching) rate during the heat treatments.

2. Compared to the sample (AT) which had been partitioned in the two salt baths, the quenched and tempered samples (WQT, OQT_1, and OQT_2) with relatively higher residual stress showed a much lower H diffusivity and permeability. On the other hand, the sub-surface H concentration (regarded simply as H solubility, C_{app}) was increased in the order of oil quenched ($OQT_1 \approx OQT_2$), water quenched (WQT), and partitioned (AT) samples. This was inconsistent with the HE index obtained by SSRT in a corrosive environment, suggesting that the H permeation data obtained under cathodic polarization cannot simulate the embrittlement phenomenon occurring in an actual corrosive environment.

3. The partitioned sample (AT) with the lowest level of localized plastic strain and dislocation density was

most susceptible to the long-term corrosion. It can also be assumed that heat treatment for the reduction of H-induced mechanical degradation may not necessarily ensure high resistance to aqueous corrosion. Therefore, the heat treatment condition should be optimized to develop an ultra-strong automotive steel with superior resistance to both corrosion and corrosion-induced HE.

Acknowledgements

References

1. J. Bian, H. Mohrbacher, J. S. Zhang, Y. T. Zhao, H. Z. Lu, and H. Dong, *Adv. Manuf.*, **3**, 27 (2015).
2. E. H. Hwang, H. G. Seong, and S. J. Kim, *Kor. J. Met. Mater.*, **56**, 570 (2018).
3. M. Tetsuya, H. Kohei, and K. Hidetaka, *JFE Technical Report*, **4**, 38 (2004).
4. J. Yang, F. Huang, Z. Guo, Y. Rong, and N. Chen, *Mater. Sci. Eng. A*, **665**, 76 (2016).
5. M. C. Jo, J. Y. Park, S. S. S, S. W. Kim, J. K. Oh, and S. H. Lee, *Mater. Sci. Eng. A*, **707**, 65 (2017).
6. S. Takagi, Y. Toji, M. Yoshino, and K. Hasegawa, *ISIJ Int.*, **52**, 316 (2012).
7. H. Karbasian and A. E. Tekkaya, *J. Mater. Process. Technol.*, **210**, 2103 (2010).
8. A. R. Ranji A. H.and Zakeri, *J. Nav. Archit. Mar. Eng.*, **7**, 93 (2010).
9. H. K. D. H. Bhadeshia, *ISIJ Int.*, **56**, 24 (2016).
10. N. Staicopolus, *J. Electrochem. Soc.*, **110**, 1121 (1963).
11. F. Farelas, M. Galicia, B. Brown, S. Nesis, and H. Castaneda, *Corros. Sci.*, **52**, 509 (2010).
12. S. Jayabal, G. Saranya, J. Wu, Y. Liu, D. Geng, and X. Meng, *J. Mater. Chem. A*, **5**, 47 (2017).
13. A. M. Mebel and D. Y. Hwang, *J. Phys. Chem. A*, **105**, 7460 (2001).
14. M. Wasim, C. Q. Li, M. Mahmoodian, and D. Robert, *J. Mater. Civ. Eng.*, **31**, 04018349-1 (2019).
15. M. Cabrini, S. Lorenzi, T. Pastore, and D. P. Bucella, *Metals*, **8**, 158 (2018).
16. J. Cwiek, *J. Achiev. Mater. Manuf. Eng.*, **37**, 193 (2009).
17. W. Hui, H. Zhang, Y. Zhang, X. Zhao, and C. Shao, *Mater. Sci. Eng. A*, **674**, 615 (2016).
18. J. Zhao, Z. Jiang, and C. S. Lee, *Corros. Sci.*, **82**, 380 (2014).
19. M. Koyama, E. Akiyama, Y. K. Lee, D. Raabe, and K. Tsuzaki, *Int. J. Hydrogen Energ.*, **42**, 12706 (2017).
20. S. A. Mujahid and H. K. D. H. Bhadeshia, *Acta. Metall. Mater.*, **40**, 389 (1992).
21. ISO 17081:2004 (E), Method of Measurement of Hydrogen Permeation and Determination of Hydrogen Uptake and Transport in Metals by an Electrochemical Technique, ISO, Switzerland (2004).
22. S. J. Kim, J. S. Park, E. H. Hwang, S. M. Ryu, H. G. Seong, and Y. R. Cho, *Int. J. Hydrogen Energ.*, **43**, 17912 (2018).
23. ASTM G129, Standard Practice for Slow Strain Rate Testing to Evaluate the Susceptibility of Metallic Materials to Environmentally Assisted Cracking (2013).
24. J. Krawczyk, P. Bala, and J. Pacyna, *J. Microsc.*, **237**, 411 (2010).
25. Y. Wang, S. Denis, B. Appolaire, and P. Archambault, *J. Phys. IV France*, **120**, 103 (2004).
26. K. H. Jack, *JISI*, **169**, 26 (1951).
27. Y. Ohmori and S. Sugisawa, *Autumn Meeting of the Japan Institute of Metals*, **12**, 170 (1971).
28. P. J. Konijnenberg, S. Zaefferer, and D. Raabe, *Acta Mater.*, **99**, 402 (2015).
29. A. Adrover, M. Hiona, L. Capobianco, P. Tripodi, and V. Violante, *J. Alloy. Comp.*, **358**, 268 (2003).
30. S. J. Kim, E. W. Yun, H. G. Jung, and K. Y. Kim, *J. Electrochem. Soc.*, **161**, 173 (2014).
31. H. K. D. H. Bhadeshia, *ISIJ Int.*, **56**, 24 (2016).
32. G. W. Hong and J. Y. Lee, *J. Mater. Sci.*, **18**, 271 (1983).
33. G. W. Hong and J. Y. Lee, *Metall. Trans. A*, **14**, 156 (1983).
34. J. S. Park, E. H. Hwang, M. J. Lee, and S. J. Kim, *Corros. Sci. Tech.*, **17**, 242 (2018).
35. E. Serra, A. Perujo, and G. Benamati, *J. Nucl. Mater.*, **245**, 108 (1997).
36. B. D. Craig, *Acta Metall.*, **25**, 1027 (1977).
37. S. J. Kim, E. H. Hwang, J. S. Park, S. M. Ryu, D. W. Yun, and H. G. Seong, *npj Mater. Degrad.*, **3**, 1 (2019).
38. J. W. Mullin, *Crystallization, 3rd ed.*, p. ?, Oxford press, Oxford, UK (1993).
39. Y. S. Kim and J. G. Kim, *Metals*, **7**, 182 (2017).